JACS
JOURNAL OF THE AMERICAN CHEMICAL SOCIETY

Article

pubs.acs.org/JACS

Are MXenes Promising Anode Materials for Li Ion Batteries? Computational Studies on Electronic Properties and Li Storage Capability of Ti_3C_2 and $Ti_3C_2X_2$ (X = F, OH) Monolayer

Qing Tang, Zhen Zhou,* and Panwen Shen

Tianjin Key Laboratory of Metal and Molecule Based Material Chemistry, Key Laboratory of Advanced Energy Materials Chemistry (Ministry of Education), Computational Centre for Molecular Science, Institute of New Energy Material Chemistry, Nankai University, Tianjin 300071, P. R. China

Supporting Information

ABSTRACT: Density functional theory (DFT) computations were performed to investigate the electronic properties and Li storage capability of Ti_3C_2, one representative MXene (M represents transition metals, and X is either C or/and N) material, and its fluorinated and hydroxylated derivatives. The Ti_3C_2 monolayer acts as a magnetic metal, while its derived $Ti_3C_2F_2$ and $Ti_3C_2(OH)_2$ in their stable conformations are semiconductors with small band gaps. Li adsorption forms a strong Coulomb interaction with Ti_3C_2-based hosts but well preserves its structural integrity. The bare Ti_3C_2 monolayer exhibits a low barrier for Li diffusion and high Li storage capacity (up to $Ti_3C_2Li_2$ stoichiometry). The surface functionalization of F and OH blocks Li transport and decreases Li storage capacity, which should be avoided in experiments. The exceptional properties, including good electronic conductivity, fast Li diffusion, low operating voltage, and high theoretical Li storage capacity, make Ti_3C_2 MXene a promising anode material for Li ion batteries.

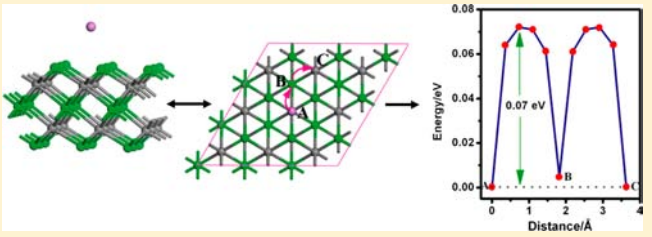

1. INTRODUCTION

Two-dimensional (2D) atomic crystals typically possess different properties from their three-dimensional (3D) bulk counterparts. Optical and electrical properties usually differ significantly due to the electron confinement effect and the absence of interlayer interactions, which, though generally weak, play an important role in determining the band structures and phonon scatterings. As an example, the single layer graphene is a zero-gap semiconductor, while the bulk graphite is a semimetal. Other differences, in mechanical properties, chemical reactivity, and so on, mainly arise from the topological effects and high surface-bulk ratios.

Despite much interest in 2D materials, there are only relatively few freestanding monolayer solids achieved in experiments. The first example was graphene.[1,2] After that, inorganic layered materials [such as hexagonal BN,[3−7] dichalcogenides ($NbSe_2$ and MoS_2),[8,9] and complex oxides ($Ba_2Sr_2CaCu_2O_x$)[10]] and metal coordination polymers (such as $[Cu_2Br(IN)_2]_n$,[11] and polymeric Fe-phthalocyanine[12]) have also been isolated as 2D single sheets via mechanical cleavage and chemical exfoliation or have been grown on substrate surface through chemical vapor deposition.[13,14] Obviously, graphene has predominated as the most studied 2D material in the past several years. Nevertheless, its simple chemistry with only carbon networking might limit its practical applications. Complex layered materials composed of more than one element may offer new opportunities due to their large variety of structural compositions that can be tuned for specific properties and applications.[15−23]

There are many types of inorganic layered materials that occur in nature or can be postsynthesized. If their 2D monolayer or few-layered structures can be isolated, the family of 2D inorganic materials should be expanded significantly. In addition to the aforementioned layered BN, dichalcogenides, complex oxides, and metal coordination polymers, MAX phases, such as layered ternary metal carbides, nitrides and carbonitrides,[24−27] which have been known for many decades dating back to early 1960s, have received renewed research interest recently.[28,29] The MAX phases have a general formula of $M_{n+1}AX_n$ (n = 1−3), where M represents transition metals (M = Ti, Sr, V, Cr, Ta, Nb, Zr, Mo, Hf), A represents the main-group sp elements (mostly IIIA or IVA, A = Al, Ga, In, Ti, Si, Ge, Sn, Pb), and X represents C or/and N. They correspond to a big family with more than 60 members and constitute a new class of layered materials with a unique combination of the properties of both metals and ceramics,[30−33] such as exceptional hardness, high melting point, excellent oxidation resistance, as well as high electrical and thermal conductivity. In addition, these MAX materials are readily machineable, relatively soft, and unusually damage-tolerant, and they can be made from inexpensive raw materials. The outstanding properties of MAX materials have aroused considerable attention in the materials community, which led to numerous technical applications.[34−36]

Received: August 26, 2012
Published: September 18, 2012

dx.doi.org/10.1021/ja308463r | J. Am. Chem. Soc. 2012, 134, 16909−16916

Structurally, MAX phases can be described as the intergrowth structures with alternative stacking of hexagonal MX layers and close-packed planar A atomic layers along the *c*-axis. However, different from graphite and many graphite-like inorganic materials (BN, MoS_2, etc.) with strong intralayer covalent bonds and weak van der Waals interlayer interactions, the MAX phases are mainly composed of a mixture of covalent, metallic, and ionic bonding, and the consequential bond strengths are quite strong. Due to their unique structural characteristics, the separation of single layers from the MAX phases cannot be easily realized with the mechanical exfoliation method as previously used in the fabrication of graphene from graphite.

Nevertheless, the synthetic challenges did not deter the researchers' enthusiasm of obtaining new 2D materials. Compared with the MX layer with exceptionally strong M−X bonds, the A-containing plane layer is relatively weakly bonded (with relatively weak interatomic A−A bonds and interlayer M−A bonds) and is thus chemically more reactive. In a recent work, taking Ti_3AlC_2 as an example, Naguib et al.[37] have developed an effective strategy to extract the Al layer from Ti_3AlC_2 without destroying the layered morphology simply by immersing Ti_3AlC_2 powers into 50% hydrofluoric acid (HF) ($Ti_3AlC_2 + 3HF = AlF_3 + {}^3/_2H_2 + Ti_3C_2$) followed by an ultrasonication in methanol. Such an as-designed route leads to the selective etching of the Al layer from the 3D layered Ti_3AlC_2 and results in the formation of exfoliated and separated Ti_3C_2 nanosheets with thickness ranging from single layer and double layers to multiple layers. Under the aqueous environment with the presence of both HF and H_2O components, the exposed Ti surfaces of the isolated Ti_3C_2 layers are initially terminated with F or/and OH groups, which can be alternatively regarded as the Al layers of the original Ti_3AlC_2 being replaced by OH or F. The obtained Ti_3C_2 nanosheets represent the first example of 2D transition metal carbides that have been successfully fabricated through the chemical exfoliation method. Following a similar procedure, other Al-containing MAX phases, including Ti_2AlC, Ta_4AlC_3, $(Ti_{0.5}Nb_{0.5})_2AlC$, $(V_{0.5}Cr_{0.5})_3AlC_2$, and Ti_3AlCN, have also been successfully exfoliated into the 2D layers of their corresponding carbides and carbonitrides, Ti_2C, Ta_4C_3, TiNbC, $(V_{0.5}Cr_{0.5})_3C_2$, and Ti_3CN_x ($x < 1$).[38]

The exfoliated 2D carbide and carbonitride nanosheets are termed as "MXene" to highlight their structural similarity to graphene. Inspired by the experimental progress, we are confident that more and more MXene materials could be exfoliated from their bulk MAX phases. As an emerging family of graphene-like inorganic analogues, the properties of MXenes are still in the early stage of explorations and are fascinating the scientific communities. Therefore, it should be of both scientific and technological importance to have a detailed understanding of their basic properties and potential applications.

In this work, we chose Ti_3C_2 as the representative MXene and performed computational investigations on the electronic properties of Ti_3C_2 monolayer with bare, fluorinated, and hydroxylated surfaces. The isolated Ti_3C_2 sheets are experimentally demonstrated to maintain the pseudoductility of Ti_3AlC_2 and exhibit high electrical conductivity, which might facilitate their potential application to electronic devices and Li ion batteries as its compositional analogue Ti_2C.[39,40] In addition, we examined the Li storage capability in the Ti_3C_2 monolayer with both bare and passivated surfaces to explore their potentials as anode materials for Li ion batteries.

2. COMPUTATIONAL DETAILS

All density functional theory (DFT) computations were performed by using the plane-wave technique as implemented in the Vienna ab initio simulation package (VASP).[41] The ion−electron interaction is described with the projector augmented wave (PAW) method.[42] A 480 eV cutoff was used for the plane-wave basis set. The exchange-correlation energy is described by the functional of Perdew, Burke, and Ernzerhof (PBE).[43] The geometry optimizations were performed by using the conjugated gradient method, and the convergence threshold was set to be 10^{-4} eV in energy and 10^{-3} eV/Å in force. The Brillouin zone was represented by Monkhorst−Pack special *k*-point mesh of 4 × 4 × 1 for geometry optimizations, while a larger grid (12 × 12 × 1) was used for electronic structure computations. To investigate the Li adsorption and diffusion on the Ti_3C_2 and $Ti_3C_2X_2$ (X = F, OH) monolayers, a 3 × 3 supercell with one adsorbed Li atom was used, and the PBE+D2 method,[44] which introduces dispersion interactions by using an empirical potential of the form C_6R, was adopted. Furthermore, the climbing-image nudged elastic band (CI-NEB) method[45] implemented in VASP was used to determine the diffusion energy barrier and the minimum energy pathways for Li diffusion on the Ti_3C_2, $Ti_3C_2F_2$, and $Ti_3C_2(OH)_2$ surfaces. This method involves optimizing a chain of images that connect the initial and final state. Each image is allowed to move only in the direction perpendicular to the hypertangent. Hence, the energy is minimized in all directions except for the reaction path.

3. RESULTS AND DISCUSSION

3.1. Structural and Electronic Properties of Monolayer Ti_3C_2 and $Ti_3C_2X_2$ (X = F, OH). First, we focused on the structural and electronic properties of monolayer Ti_3C_2 as well as its fluorinated and hydroxylated derivatives [denoted as $Ti_3C_2F_2$ and $Ti_3C_2(OH)_2$, respectively]. As a starting point of geometry optimizations, the atomic model of the free-standing Ti_3C_2 sheet is constructed from the Ti_3AlC_2 phase. Each Ti_3C_2 monolayer is built up of quintuple layers stacked in a sequence of Ti(1)−C−Ti(2)−C−Ti(1), which can be described as the three Ti-atomic layers being intercleaved with two C-atomic layers forming edge-shared Ti_6C octahedral (Figure 1a, left). The fluorinated and hydroxylated Ti_3C_2 sheets are constructed accordingly by saturating the surface under-coordinated Ti(1) atoms with F and OH, respectively. Herein, three major possible configurations of F and OH termination modes are considered: for type I (Figure 1b,e), all the F or OH groups are located above the hollow sites between the three neighboring C atoms or point directly toward the Ti(2) atoms on both sides of Ti_3C_2 layer; for type II (Figure 1c,f), all the F or OH groups are oriented above the topmost sites of C atoms on both sides of the Ti_3C_2 layer; type III structure (Figure 1d,g) can be viewed as a combination of both types I and II, in which the F or OH groups are placed above the hollow sites of C atoms on one side and above the top sites of C atoms on the other side, forming an asymmetric arrangement on the two sides of the Ti_3C_2 layer. The structural relaxations of all the free-standing Ti_3C_2, (I-, II-, III-)$Ti_3C_2F_2$, and (I-, II-, III-)$Ti_3C_2(OH)_2$ monolayers have well preserved the geometrical integrity of the original layers.

The Ti_3C_2 layer has a magnetic ground state with a total magnetic moment of about 1.93 μ_B per unit cell, while the $Ti_3C_2F_2$ and $Ti_3C_2(OH)_2$ are ground-state nonmagnetic. The spin density distribution (Figure 1a, middle) indicates that the induced magnetism of Ti_3C_2 originates from the dangling 3d orbitals of the surface Ti atoms. The surface nearest Ti(1)−C bond length of the bare Ti_3C_2 sheet (2.064 Å) is slightly shorter than that of the bulk Ti_3AlC_2 phase (2.089 Å). After F and OH saturation, the surface Ti(1)−C bond length is elongated to

dx.doi.org/10.1021/ja308463r | J. Am. Chem. Soc. 2012, 134, 16909−16916

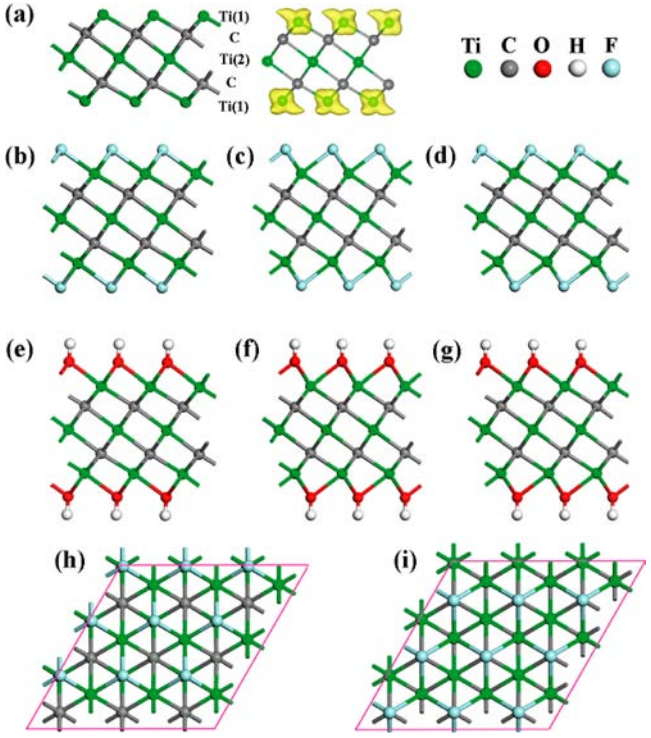

Figure 1. Optimized geometries of the free-standing Ti_3C_2 monolayer and its fluorinated and hydroxylated structural forms: (a) side view of the bare Ti_3C_2 monolayer composed of a quintuple layer with Ti(1)−C−Ti(2)−C−Ti(1) stacking modes (left) and the computed spin density distribution (middle); side views of (b) I-$Ti_3C_2F_2$, (c) II-$Ti_3C_2F_2$, (d) III-$Ti_3C_2F_2$, (e) I-$Ti_3C_2(OH)_2$, (f) II-$Ti_3C_2(OH)_2$, and (g) III-$Ti_3C_2(OH)_2$; (h and i) the top views of I-$Ti_3C_2F_2$ and II-$Ti_3C_2F_2$, in which the F groups are located above the hollow sites between the three neighboring C atoms and above the topmost C atoms, respectively. III-$Ti_3C_2F_2$ is a combination of I-$Ti_3C_2F_2$ and II-$Ti_3C_2F_2$, in which the F groups are located at the hollow sites on one side and at the C atoms on the other side. The geometrical arrangements of OH groups for I-$Ti_3C_2(OH)_2$, II-$Ti_3C_2(OH)_2$, and III-$Ti_3C_2(OH)_2$ are structurally similar to their fluorinated analogues.

2.081 Å (I-$Ti_3C_2F_2$), 2.107 Å (II-$Ti_3C_2F_2$), 2.074 Å (2.110 Å) (III-$Ti_3C_2F_2$), 2.087 Å [I-$Ti_3C_2(OH)_2$], 2.104 Å [II-$Ti_3C_2(OH)_2$], and 2.083 Å (2.112 Å) [III-$Ti_3C_2(OH)_2$], respectively. The average Ti(1)−F bond lengths are relaxed to 2.167 Å (I-$Ti_3C_2F_2$), 2.197 Å (II-$Ti_3C_2F_2$), and 2.163 (2.203) Å (III-$Ti_3C_2F_2$), respectively, and the average Ti(1)−O bond lengths are optimized to 2.192 Å [I-$Ti_3C_2(OH)_2$], 2.202 Å [II-$Ti_3C_2(OH)_2$], and 2.178 (2.205) Å [III-$Ti_3C_2(OH)_2$], respectively.

The structural stability of different $Ti_3C_2F_2$ and $Ti_3C_2(OH)_2$ configurations can be estimated by comparing their relative total energies. For both $Ti_3C_2F_2$ and $Ti_3C_2(OH)_2$, type I conformer is energetically most favorable. Specifically, I-$Ti_3C_2F_2$ is energetically lower than II-$Ti_3C_2F_2$ and III-$Ti_3C_2F_2$ by about 0.79 and 0.40 eV per unit cell, respectively, while I-$Ti_3C_2(OH)_2$ is energetically lower than II-$Ti_3C_2(OH)_2$ and III-$Ti_3C_2(OH)_2$ by about 0.51 and 0.25 eV per unit cell, respectively. This suggests that both F and OH groups tend to attach the hollow sites between the three neighboring carbon atoms, and the lowest structural stability of type II conformers should be ascribed to the steric repulsion between F or OH groups with the underneath carbon atoms.

The electronic properties of Ti_3C_2 layers are strongly associated with the surface terminations. The computed band structure of the bare Ti_3C_2 monolayer (Figure 2a) is characterized as a magnetic metal, in which the spin-up and spin-down channels are split and both are turned into metallicity with substantial electron states crossing the Fermi level. The previous report also revealed a metallic-like state for the free-standing Ti_3C_2 layer,[46] though spin polarization was not considered.

Interestingly, when terminated with F and OH, the resultant $Ti_3C_2F_2$ and $Ti_3C_2(OH)_2$ monolayers show versatile conducting characteristics, which can be narrow-band gap semiconductors or metals, depending strongly on the spatial arrangements of surface F and OH groups. In the case of surface fluorination, the electronic structure of the most stable I-$Ti_3C_2F_2$ (Figure 2b) exhibits a semiconducting state with a prominently narrow band gap of about 0.04 eV. III-$Ti_3C_2F_2$ (Figure 2d) remains also semiconducting like I-$Ti_3C_2F_2$, and the resulting band gap is also small (0.03 eV). In contrast, II-$Ti_3C_2F_2$ (Figure 2c) is a metal, in which there are substantial electron states around the Fermi level. With surface hydroxylation, the band structure of the most favorable I-$Ti_3C_2(OH)_2$ (Figure 2e) has a semiconducting character, with a clear separation of the valence band and conduction band near the Fermi level by about 0.05 eV. III-$Ti_3C_2(OH)_2$ (Figure 2g) preserves the semiconducting behavior of I-$Ti_3C_2(OH)_2$ and possesses a narrow band gap of about 0.07 eV. However, II-$Ti_3C_2(OH)_2$ (Figure 2f) is metallic with finite electronic states crossing the Fermi level. Therefore, the electronic properties of Ti_3C_2 monolayer can be modified by varying the surface functional groups and their geometrical conformations. The semiconducting behaviors predicted for the I-$Ti_3C_2F_2$ and I-$Ti_3C_2(OH)_2$ conformers are in good agreement with previous results.[37]

3.2. Li Adsorption and Diffusion on Monolayer Ti_3C_2 and $Ti_3C_2X_2$ (X = F, OH). Ti_3C_2 monolayer has a metallic character, and its fluorinated or hydroxylated derivatives in their stable forms are narrow-band gap semiconductors. Compared with many transition-metal oxides with semiconducting or insulating conductivity, the metallic or narrow-band gap semiconducting properties offer an intrinsic advantage in electrical conductivity, which may facilitate the fundamental science and technological breakthrough of Ti_3C_2 and its functionalized derivatives in electronics and energy storage applications. Therefore, after the thorough understanding on the basic electronic properties of Ti_3C_2, $Ti_3C_2F_2$, and $Ti_3C_2(OH)_2$, we subsequently extended our computations to the aspects of Li adsorption and diffusion behaviors on Ti_3C_2 as well as its F- and OH-functionalized structures. Hereafter only the stable conformers, I-$Ti_3C_2F_2$ and I-$Ti_3C_2(OH)_2$, were considered.

In evaluating Li adsorption on Ti_3C_2 and its related hosts, it is important to know exactly the favorable locations for Li adsorption first. Since the Li insertion into the inner interstitial cube-center sites can lead to significant volume expansion accompanied by the Ti−C bond breaking, which results in the disruption of the structural integrity and an endothermic Li adsorption, we mainly considered Li occupation at the surface sites. Here a simulated 3 × 3 supercell with one adsorbed Li atom was used to investigate the Li adsorption, which corresponds to a chemical stoichiometry of $Ti_{27}C_{18}Li$, $Ti_{27}C_{18}F_{18}Li$, and $Ti_{27}C_{18}(OH)_{18}Li$, respectively.

dx.doi.org/10.1021/ja308463r | J. Am. Chem. Soc. 2012, 134, 16909−16916

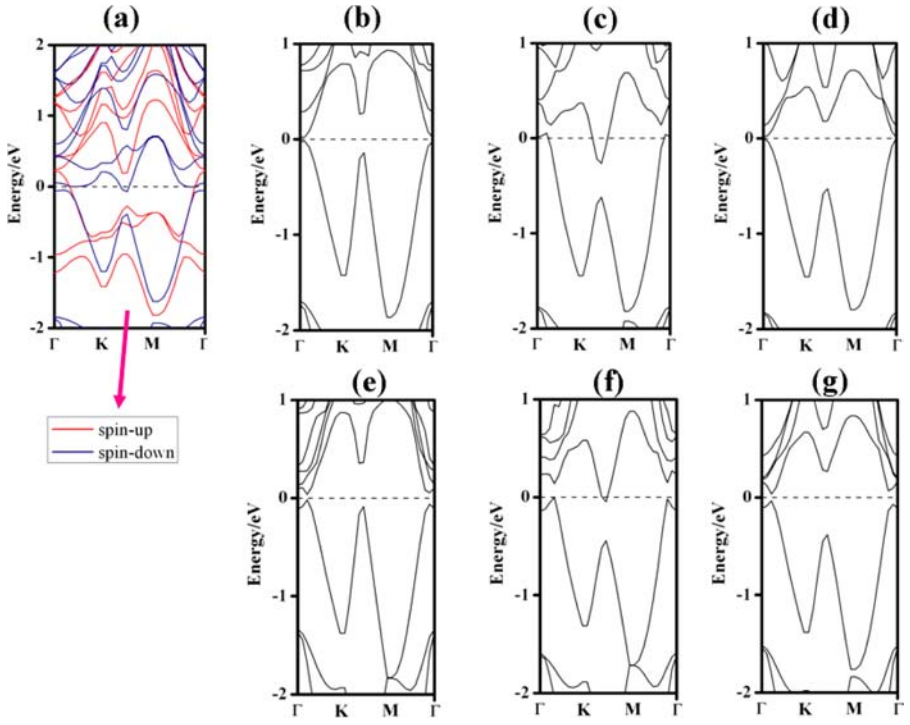

Figure 2. Band structures near the Fermi level for the Ti_3C_2 monolayer (a), I-$Ti_3C_2F_2$ (b), II-$Ti_3C_2F_2$ (c), III-$Ti_3C_2F_2$ (d), I-$Ti_3C_2(OH)_2$ (e), II-$Ti_3C_2(OH)_2$ (f), and III-$Ti_3C_2(OH)_2$ (g). For Ti_3C_2, the spin-polarized band structures with both spin-up and spin-down channels are presented.

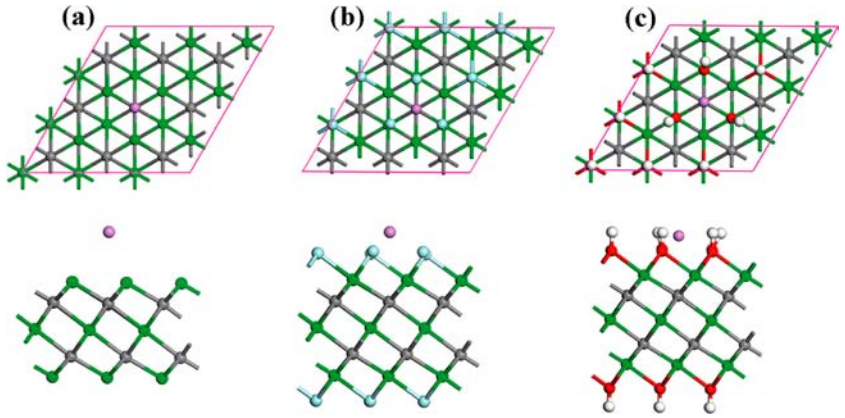

Figure 3. Top and side views of the optimized Li-adsorbed Ti_3C_2 (a), I-$Ti_3C_2F_2$ (b), and I-$Ti_3C_2(OH)_2$ (c) monolayers.

To analyze the surface adsorption of Li on Ti_3C_2, I-$Ti_3C_2F_2$, and I-$Ti_3C_2(OH)_2$, three types of sites with high symmetry were considered: the site on top of the Ti(1) atom, the site on top of the C atom, and the site on top of the Ti(2) atom (for Ti_3C_2), F atom (for I-$Ti_3C_2F_2$), and OH groups (for I-$Ti_3C_2(OH)_2$), respectively. The adsorption energy (eV/Li atom) is defined as the difference between the total energy of the complex system in which the Li atom is adsorbed on Ti_3C_2 [I-$Ti_3C_2F_2$, I-$Ti_3C_2(OH)_2$] and the sum of the total energy of the isolated Li atom (belonging to Li metal crystal, with body-centered cubic structure and a lattice constant of 3.491 Å) and the isolated Ti_3C_2 [I-$Ti_3C_2F_2$, I-$Ti_3C_2(OH)_2$] monolayer of a 3 × 3 supercell.

For all three of the examined structures, the most favorable adsorption configurations are that the Li atoms are adsorbed on top sites of the C atoms (Figure 3). The optimal distance between Li and C atoms (Li−C spatial separation) and the resultant adsorption energy with respect to Ti_3C_2, I-$Ti_3C_2F_2$, and I-$Ti_3C_2(OH)_2$ monolayer are 3.535, 3.459, 3.126 Å and −0.504, −0.951, −0.201 eV/Li atom, respectively. Moreover, in the relaxed structures, the average nearest-neighbor Li−Ti(1), Li−F, and Li−O distances with respect to the Li-adsorbed Ti_3C_2, I-$Ti_3C_2F_2$, and I-$Ti_3C_2(OH)_2$ monolayers are 3.023, 1.901, and 1.898 Å, respectively. The Li adsorption on I-$Ti_3C_2F_2$ and I-$Ti_3C_2(OH)_2$ leads to the localized geometric changes, where the three nearest-neighbor F atoms tend to point slightly inward toward the adsorbed Li atom, whereas the three nearest-neighbor OH groups tend to point outward toward the adsorbed Li atom.

To get further insight into the interactions between Li and Ti_3C_2 [I-$Ti_3C_2F_2$, I-$Ti_3C_2(OH)_2$] monolayers, we computed the density of states (DOS) of Ti_3C_2, I-$Ti_3C_2F_2$, and I-$Ti_3C_2(OH)_2$ monolayers with the adsorbed Li (Figure 4). Generally, the Li adsorption does not significantly change the overall DOS structures of pristine Ti_3C_2, I-$Ti_3C_2F_2$, and I-$Ti_3C_2(OH)_2$, except for the upshift of Fermi level of Ti_3C_2 and

dx.doi.org/10.1021/ja308463r | J. Am. Chem. Soc. 2012, 134, 16909−16916

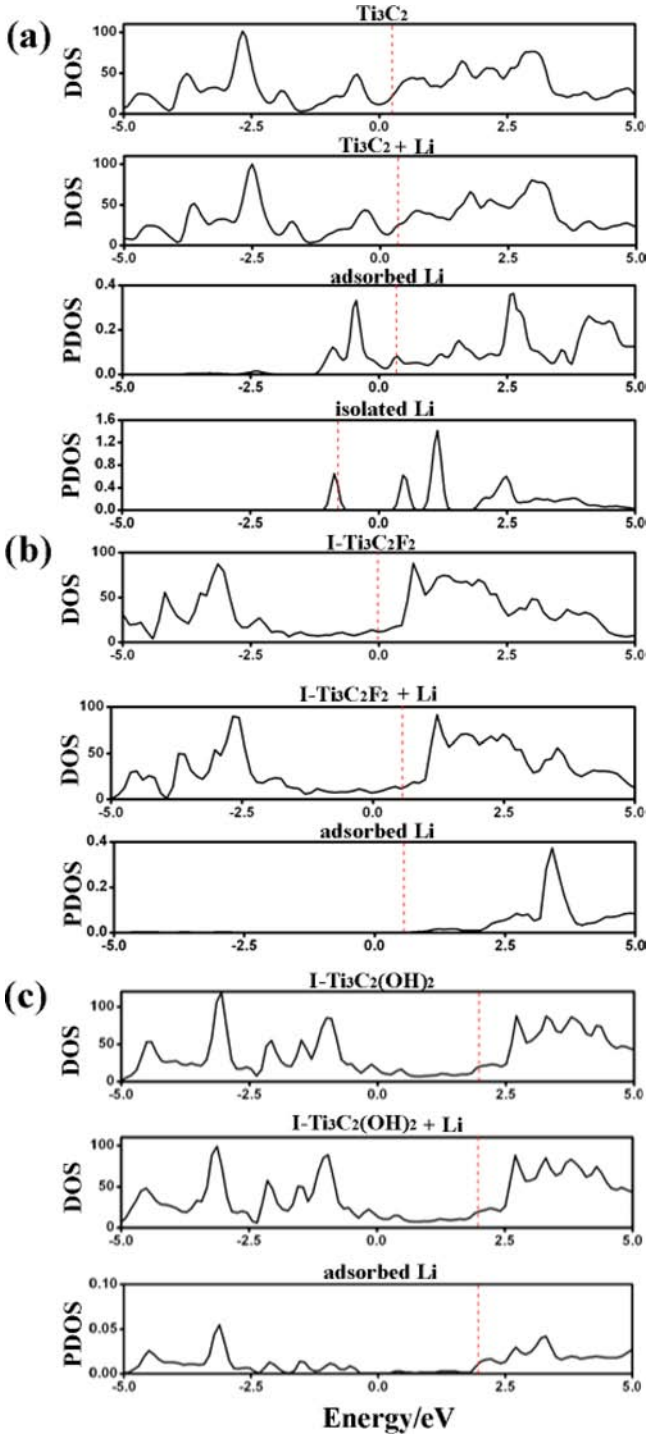

Figure 4. (a) Density of states (DOS) of bare Ti_3C_2 and the Li-adsorbed Ti_3C_2, along with the partial density of states (PDOS) of adsorbed Li and isolated Li atom. (b and c) The total DOS of bare I-$Ti_3C_2F_2$, Li-adsorbed I-$Ti_3C_2F_2$, bare I-$Ti_3C_2(OH)_2$, and Li-adsorbed I-$Ti_3C_2(OH)_2$, together with the PDOS of the adsorbed Li atom, respectively. The red dotted lines denote the locations of the Fermi level.

I-$Ti_3C_2F_2$ upon Li adsorption. The Fermi level nearly does not shift in the case of I-$Ti_3C_2(OH)_2$ after Li adsorption. For the Li-adsorbed Ti_3C_2, I-$Ti_3C_2F_2$, and I-$Ti_3C_2(OH)_2$, the partial density of states (PDOS) of Li atom indicates a small or nearly negligible electron state near the Fermi level, and the Li atoms mainly contribute to the valence band and conduction band. However, there is a substantial electron state near the Fermi level for the isolated Li atom. This indicates that the adsorbed Li atom becomes partially or fully ionized, and thus, the Coulomb interaction between Li and Ti_3C_2, I-$Ti_3C_2F_2$, or I-$Ti_3C_2(OH)_2$ should be governed by charge transfer. Bader charge analysis based on the electronic charge density shows that the adsorbed Li atom acts as an electron donor, and about 0.22, 0.41, and 0.33 *|e|* are transferred to the underlying Ti_3C_2, I-$Ti_3C_2F_2$, and I-$Ti_3C_2(OH)_2$ substrate, respectively. According to the above discussion and analysis, the high adsorption energies and the large charge transfer suggest that the adsorbed Li can form a strong Coulomb interaction with Ti_3C_2, I-$Ti_3C_2F_2$, and I-$Ti_3C_2(OH)_2$ monolayers.

The diffusion path and barrier of Li on Ti_3C_2, I-$Ti_3C_2F_2$, and I-$Ti_3C_2(OH)_2$ surface are indispensable to evaluate their potentials in Li ion batteries. In order to figure out the migration pathways for Li ions, three possible spatial hopping pathways with high structural symmetry between the two nearest neighboring Li adsorption sites were explored (Figure 5a,b): for pathway I, the Li ion is allowed to move directly to the nearest neighboring site in a one-step linear path (top C→ top C); for pathway II, the Li ion is designed to move along the pathway from the site on top of C atoms to the one on top of Ti(1) atoms and then to the nearest neighboring C atoms (top C→top Ti(1)→top C); for pathway III, the Li ion is moved along the pathway from top C→top Ti(2) (for Li adsorbed Ti_3C_2), top F (for Li adsorbed I-$Ti_3C_2F_2$), or top OH groups (for Li adsorbed I-$Ti_3C_2(OH)_2$)→top C. For I-$Ti_3C_2(OH)_2$, we only considered the Li diffusion along pathways II and III (Figure 5c), since the Li migration along pathway I leads to a significant spatial repulsion between Li and the OH groups, which is energetically unfavorable and can result in the O−H bond breakage.

For the bare Ti_3C_2 sheet (Figure 5d), pathways I and III have the lowest diffusion barrier of about 0.07 eV and correspond to the path lengths of about 0.762 and 0.727 Å, respectively, while pathway II exhibits a much higher energy barrier (up to 0.18 eV). Particularly, there is a local energy-minimum point along pathway III, which is virtually located at the top Ti(2) site with a Li−Ti(2) distance of 4.801 Å and is only energetically higher than the adsorption ground-state at the top C site by about 0.005 eV. The local minimum for pathway I is about 0.05 eV higher than the adsorption ground state and located at the bridge site above the C−Ti(2) bond with a Li−C distance of 3.825 Å. At the barrier state along pathway III, the Li ion is located at the bridge site above the C−Ti(2) bond with a Li−C separation of about 3.614 Å (Figure 5d, lower part). The barrier state along pathway I is also located above the C−Ti(2) bond with a comparable Li−C distance of about 3.610 Å. Actually, the energetically optimized pathway I does not follow the predesigned linear pathway, but is nearly analogous to that of the optimized pathway III, which means that the Li ion prefers to migrate along the C→Ti(2)→C pathway, and this could also explain similar energy barriers and barrier state configurations for both pathways I and III.

Similarly, for the case of Li diffusion on I-$Ti_3C_2F_2$, the relaxed pathway I also does not straightly follow the originally proposed linear path from C→C but rather goes through the C→Ti(1)→C pathway, in analogy with the relaxed pathway II. By a similar analysis, the Li diffusion on I-$Ti_3C_2F_2$ following pathways I and II exhibits a comparable energy barrier of 0.36 eV, and the corresponding path lengths are about 1.257 and 1.156 Å, respectively. The local minimum along pathways I and

dx.doi.org/10.1021/ja308463r | J. Am. Chem. Soc. 2012, 134, 16909−16916

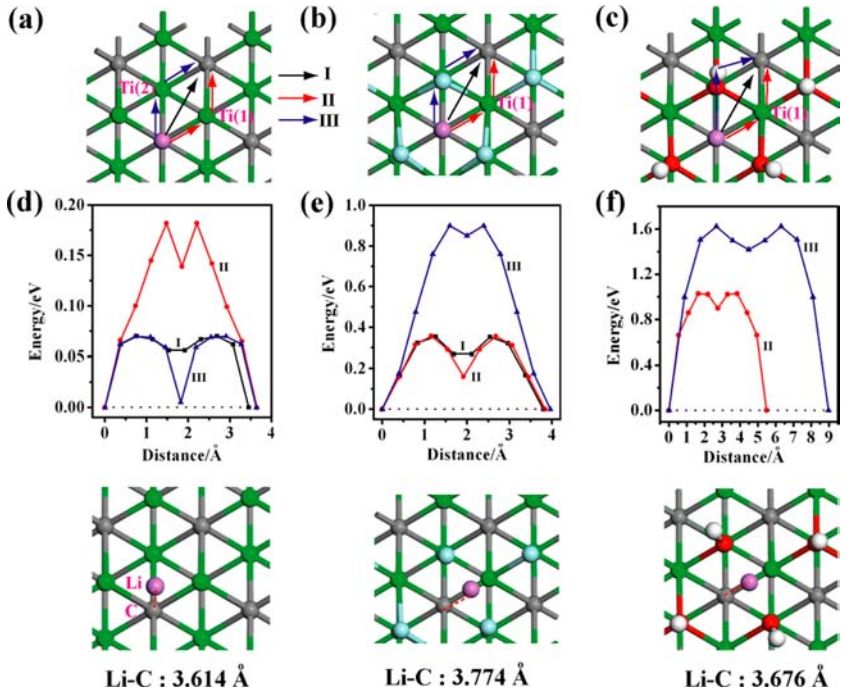

Figure 5. Schematic representations of the top view of the considered migration paths for Li diffusion on Ti_3C_2 (a), I-$Ti_3C_2F_2$ (b), and I-$Ti_3C_2(OH)_2$ (c) monolayer, where the black, red, and blue line represent pathways I, II, and III, respectively. Below are the corresponding diffusion barrier profiles of Li on Ti_3C_2 (d), I-$Ti_3C_2F_2$ (e), and I-$Ti_3C_2(OH)_2$ (f) monolayer through the predesigned pathways, and the lowest part shows the local atomic configuration at the barrier state that is associated with the optimal diffusion path with the lowest energy barrier.

II is located at the bridge site above the C−Ti(1) bond (with Li−C distance of 3.922 Å) and at the top Ti(1) atom [with Li−Ti(1) distance of 2.614 Å], exhibiting an energy barrier height of 0.27 and 0.16 eV, respectively. Moreover, the barrier state with respect to pathways I and II is located above the C−Ti(1) bond with a Li−C distance of 3.799 and 3.774 Å (Figure 5e, lower part), respectively.

For the case of I-$Ti_3C_2(OH)_2$, only two different migration pathways were examined: the Li diffusion through pathway II has a lower barrier (1.02 eV) than that of pathway III (1.62 eV). The barrier state along pathway II has a path length of 1.646 Å, and the resulting configuration is located above the C−Ti(1) bond with a Li−C distance of 3.676 Å. Similar to the case in I-$Ti_3C_2F_2$, the local minimum for Li diffusion on I-$Ti_3C_2(OH)_2$ along pathway II is also identified to be on top of the Ti(1) atom, in which the Li ion is located about 2.536 Å from the Ti(1) atom, and the corresponding energy barrier is 0.90 eV.

By comparing the predicted diffusion barriers and the related path lengths of the three systems, we can conclude that the Li diffusion follows the order Ti_3C_2 > I-$Ti_3C_2F_2$ > I-$Ti_3C_2(OH)_2$, in which the Li ion migrates more easily and freely on the Ti_3C_2 surface due to its lowest energy barrier and the shortest path length, and thus, the Ti_3C_2 monolayer has the best high-rate performance for Li transport. The higher diffusion barrier on I-$Ti_3C_2F_2$ and I-$Ti_3C_2(OH)_2$ should be ascribed to the steric hindrance induced by the surface F and OH groups, and the larger OH groups would generate a comparatively higher blockage for Li migration during the lithiation process.

3.3. Average Open Circuit Voltage and Theoretical Li Storage Capacity of Monolayer Ti_3C_2 and $Ti_3C_2X_2$ (X = F, OH). The above discussion only considered one adsorbed Li atom, and the real Li adsorption and diffusion processes should accommodate more Li atoms forming a cumulative effect. In order to evaluate the average open circuit voltage and the theoretical Li storage capacity of the free-standing Ti_3C_2 monolayer and its derivatives, it is necessary to estimate the Li adsorption capacity with the possible maximum accommodations, and here we considered the 2 × 2 supercell with increased Li atoms on the surface of the hosts.

Our computations reveal that the 2 × 2 supercell of Ti_3C_2, I-$Ti_3C_2F_2$, and I-$Ti_3C_2(OH)_2$ monolayer can accommodate up to eight, four, and two Li atoms, which correspond to the chemical stoichiometry of $Ti_3C_2Li_2$, I-$Ti_3C_2F_2Li$, and I-$Ti_3C_2(OH)_2Li_{0.5}$, respectively. The lower Li capacity in I-$Ti_3C_2F_2$ and I-$Ti_3C_2(OH)_2$ should be attributed to the steric effect, in which the presence of surface groups can impede the spatial occupancy of more Li ions, and otherwise, the surface F or OH groups would be repulsed, leading to the formation of LiF or LiOH side products.

A number of electrochemical properties were then derived directly from the difference in total energies before and after Li intercalation. Typically, the anode charge/discharge processes assume the following half-cell reaction vs Li/Li^+:

$$Ti_3C_2[\text{I-}Ti_3C_2F_2,\ \text{I-}Ti_3C_2(OH)_2] + xLi^+ + xe^- \leftrightarrow Ti_3C_2[\text{I-}Ti_3C_2F_2,\ \text{I-}Ti_3C_2(OH)_2]Li_x$$

The open circuit voltage (OCV) for an intercalation reaction involving xLi^+ ions can then be computed from the energy difference if volume and entropy effects are neglected:[47−50]

$$OCV \approx \{E[Ti_3C_2,\ \text{I-}Ti_3C_2F_2,\ \text{I-}Ti_3C_2(OH)_2] + xE(Li) - E[Ti_3C_2Li_x,\ \text{I-}Ti_3C_2F_2Li_x,\ \text{I-}Ti_3C_2(OH)_2Li_x]\}/x$$

Herein, the OCVs were computed for the case of $x = 2$ for $Ti_3C_2Li_2$, $x = 1$ for I-$Ti_3C_2F_2Li$, and $x = 0.5$ for I-

dx.doi.org/10.1021/ja308463r | J. Am. Chem. Soc. 2012, 134, 16909−16916

$Ti_3C_2(OH)_2Li_{0.5}$. Turning to the battery-related properties, the computed OCV is 0.62, 0.56, and 0.14 V for $Ti_3C_2Li_2$, I-$Ti_3C_2F_2Li$, and I-$Ti_3C_2(OH)_2Li_{0.5}$, respectively, and the corresponding theoretical specific capacity provided by the above structures should be 320 (the same as the prediction in a previous report[37]), 130, and 67 mAh g^{-1}, respectively. This indicates that surface functionalizations reduce the open circuit voltage, which is advantageous for their applications as anode materials in Li ion batteries; however, their specific capacity and rate-performance will decrease as compared with the bare Ti_3C_2 monolayer. Moreover, the surface F/OH groups are sensitive to Li adsorption, and the increased Li occupancy will lead to the surface instability and thus reduce the reversibility and cyclic stability of Ti_3C_2 anodes. Therefore, it should be in principle necessary to avoid the surface functionalizations in the realistic synthetic procedures to improve the electrochemical performances of Ti_3C_2.

Compared with commercial anode materials based on TiO_2 polymorphs,[51,52] which are limited by their poor electrical conductivity, high operating voltage (between 1.5−1.8 V),[53,54] and low specific capacity (<200 mAh g^{-1}), but are still considered viable anode candidates due to their high safety and cyclic stability, the 2D Ti_3C_2 monolayer is applicably more advantageous than TiO_2 due to its enhanced electronic conductivity (metallic characteristic), decreased open circuit voltage, and improved Li storage capacity. Also, the predicted diffusion barrier (0.07 eV) for an isolated Li atom on the Ti_3C_2 is much lower than that in the anatase TiO_2 (0.35−0.65 eV) determined theoretically and experimentally,[55−61] which means that Ti_3C_2 monolayer can exhibit faster Li transport and higher charge/discharge rates than the TiO_2 anode. Another commercial anode material, graphite, is a semimetal with a specific Li storage capacity of 372 mAh g^{-1} (LiC_6) and a low operation voltage of ∼0.2 eV. Theoretical studies[62−64] indicated that the Li diffusion within the graphite interlayers needs to overcome an energy barrier of ∼0.3 eV. Therefore, Ti_3C_2 monolayer exhibits much lower barrier for Li diffusion; however, its specific capacity and operation voltage are less advantageous than those of graphite. The electrochemical properties predicted by DFT computations disclose that Ti_3C_2 monolayer is a promising alternative for TiO_2 anode materials in Li ion batteries.

4. CONCLUSION

In summary, based on density functional theory (DFT) computations, we systematically investigated the structural stability and electronic properties of the experimentally realized 2D Ti_3C_2 sheet and its F- or OH-functionalized forms, and then explored the potentials of Ti_3C_2-related materials as Li ion battery anodes. The bare Ti_3C_2 sheet behaves as a magnetic metal, while $Ti_3C_2F_2$ and $Ti_3C_2(OH)_2$ can be narrow-band gap semiconductors or metals depending strongly on how the surface F and OH groups are geometrically terminated. In the most stable forms, the F and OH groups prefer to be located above the hollow sites between the three neighboring C atoms, and the resulting I-$Ti_3C_2F_2$ and I-$Ti_3C_2(OH)_2$ are all semiconductors with tremendously small band gaps.

The metallic or narrow-band gap semiconducting characteristics favor the potential applications of Ti_3C_2-related materials to Li ion batteries. For the bare Ti_3C_2 monolayer, its combined extraordinary properties, including good electrical conductivity, low diffusion barrier, low open circuit voltage, and high theoretical Li capacity, offer it great potential as an alternative anode material to TiO_2 in Li ion batteries. For its fluorinated and hydroxylated derivatives, however, the surface functionalization tends to degrade the Li diffusion and decrease the Li storage capacity and thus should be avoided in the practical synthetic experiments. Our results give insightful prospects for experimental peers in exploring the potentials of Ti_3C_2 as electronic and energy storage materials.

Noteworthy, the Ti_3C_2 monolayer only represents one example of the new family of MXenes, and the implications of this work can be helpful to design more MXenes with better performances. Further experimental and computational investigations on MXenes are highly desirable to shed light on their prospects as advanced materials.

■ ASSOCIATED CONTENT

Supporting Information

Optimized geometries and energies of all the structures involved in this work. This material is available free of charge via the Internet at http://pubs.acs.org.

■ AUTHOR INFORMATION

Corresponding Author

zhouzhen@nankai.edu.cn

Notes

The authors declare no competing financial interest.

■ ACKNOWLEDGMENTS

This work was supported by NSFC (21073096), the 111 Project (B12015), and the Fundamental Research Funds for the Central Universities in China. The computations were performed on TianHe-1(A) at the National Supercomputer Center in Tianjin and Magic Cube at Shanghai Supercomputer Center.

■ REFERENCES

(1) Novoselov, K. S.; Geim, A. K.; Morozov, S. V.; Jiang, D.; Zhang, Y.; Dubonos, S. V.; Grigorieva, I. V.; Firsov, A. A. *Science* **2004**, *306*, 666−669.

(2) Geim, A. K.; Novoselov, K. S. *Nat. Mater.* **2007**, *6*, 183−191.

(3) Pacilé, D.; Meyer, J. C.; Girit, Ç. Ö.; Zettl, A. *Appl. Phys. Lett.* **2008**, *92*, 133107.

(4) Han, W.-Q.; Wu, L.; Zhu, Y.; Watanabe, K.; Taniguchi, T. *Appl. Phys. Lett.* **2008**, *93*, 223103.

(5) Jin, C.; Lin, F.; Suenaga, K.; Iijima, S. *Phys. Rev. Lett.* **2009**, *102*, 195505.

(6) Lin, Y.; Williams, T. V.; Connell, J. W. *J. Phys. Chem. Lett.* **2010**, *1*, 277−283.

(7) Zeng, H. B.; Zhi, C. Y.; Zhang, Z. H.; Wei, X. L.; Wang, X. B.; Guo, W. L.; Bando, Y.; Golberg, D. *Nano Lett.* **2010**, *10*, 5049−5055.

(8) Zhou, K, -G.; Mao, N, -N.; Wang, H, -X.; Peng, Y.; Zhang, H, -L. *Angew. Chem., Int. Ed.* **2011**, *50*, 10839−10842.

(9) Zeng, Z.; Yin, Z.; Huang, X.; Li, H.; He, Q.; Lu, G.; Boey, F.; Zhang, H. *Angew. Chem., Int. Ed.* **2011**, *50*, 11093−11097.

(10) Novoselov, K. S.; Jiang, D.; Schedin, F.; Booth, T. J.; Khotkevich, V. V.; Morozov, S. V.; Geim, A. K. *Proc. Natl. Acad. Sci. U. S. A.* **2005**, *102*, 10451−10453.

(11) Amo-Ochoa, P.; Welte, L.; González-Prieto, R.; Sanz Miguel, P. J.; Gó mez-García, C. J.; Mateo-Martí, E.; Delgado, S.; Gómez-Herrero, J.; Zamora, F. *Chem. Commun.* **2010**, *46*, 3262−3264.

(12) Abel, M.; Clair, S.; Ourdjini, O.; Mossoyan, M.; Porte, L. *J. Am. Chem. Soc.* **2011**, *133*, 1203−1205.

(13) Mas-Ballesté, R.; Gómez-Navarro, C.; Gómez-Herrero, J.; Zamora, F. *Nanoscale* **2011**, *3*, 20−30.

(14) Coleman, J. N.; Lotya, M.; O'Neill, A.; Bergin, S. D.; King, P. J.; Khan, U.; Young, K.; Gaucher, A.; De, S.; Smith, R. J.; Shvets, I. V.;

Arora, S. K.; Stanton, G.; Kim, H.-Y.; Lee, K.; Kim, G. T.; Duesberg, G. S.; Hallam, T.; Boland, J. J.; Wang, J. J.; Donegan, J. F.; Grunlan, J. C.; Moriarty, G.; Shmeliov, A.; Nicholls, R. J.; Perkins, J. M.; Grieveson, E. M.; Theuwissen, K.; McComb, D. W.; Nellist, P. D.; Nicolosi, V. *Science* **2011**, *331*, 568−571.
(15) Tang, Q.; Zhou, Z.; Chen, Z. F. *J. Phys. Chem. C* **2011**, *115*, 18531−18537.
(16) Chen, W.; Li, Y. F.; Yu, G. T.; Li, C. Z.; Zhang, S. B.; Zhou, Z.; Chen, Z. F. *J. Am. Chem. Soc.* **2010**, *132*, 1699−1705.
(17) Tang, Q.; Cui, Y.; Li, Y. F.; Zhou, Z.; Chen, Z. F. *J. Phys. Chem. C* **2011**, *115*, 1724−1731.
(18) Li, Y. F.; Zhou, Z.; Zhang, S. B.; Chen, Z. F. *J. Am. Chem. Soc.* **2008**, *130*, 16739−16744.
(19) Li, Y. F.; Wu, D. H.; Zhou, Z.; Cabrera, C. R.; Chen, Z. F. *J. Phys. Chem. Lett.* **2012**, *3*, 2221−2227.
(20) Tang, Q.; Li, F. Y.; Zhou, Z.; Chen, Z. F. *J. Phys. Chem. C* **2011**, *115*, 11983−11990.
(21) Tang, Q.; Li, Y. F.; Zhou, Z.; Chen, Y. S.; Chen, Z. F. *ACS Appl. Mater. Interfaces* **2010**, *2*, 2442−2447.
(22) Li, Y. F.; Li, F. Y.; Zhou, Z.; Chen, Z. F. *J. Am. Chem. Soc.* **2011**, *133*, 900−908.
(23) Tang, Q.; Zhou, Z.; Chen, Z. F. *J. Phys. Chem. C* **2012**, *116*, 4119−4125.
(24) Lengauer, W. Transition Metal Carbides, Nitrides, and Carbonitrides. In *Handbook of Ceramic Hard Materials*, 1 ed.; Riedel, R.; Wiley-VCH, Weinheim, Germany, 2000, 202−252.
(25) Barsoum, M. W. *Prog. Solid State Chem.* **2000**, *28*, 201−281.
(26) Hfgberg, H.; Hultman, L.; Emmerlich, J.; Joelsson, T.; Eklund, P.; Molina-Aldareguia, J. M.; Palmquist, J. -P.; Wilhelmsson, O.; Jansson, U. *Surf. Coat. Technol.* **2005**, *193*, 6−10.
(27) Wang, J.; Zhou, Y. *Annu. Rev. Mater. Sci.* **2009**, *39*, 415−443.
(28) Keast, V. J.; Harris, S.; Smith, D. K. *Phys. Rev. B* **2009**, *80*, 214113.
(29) Ahuja, R.; Eriksson, O.; Wills, J. M.; Johansson, B. *Appl. Phys. Lett.* **2000**, *76*, 2226−2228.
(30) Zhang, H. B.; Zhou, Y. C.; Bao, Y. W.; Wang, J. Y. *J. Mater. Res.* **2006**, *21*, 402−408.
(31) Zhang, H. B.; Zhou, Y. C.; Bao, Y. W.; Li, M. S. *J. Mater. Res.* **2006**, *21*, 2401−2407.
(32) Barsoum, M. W.; El-Raghy, T. *J. Am. Ceram. Soc.* **1996**, *79*, 1953−1956.
(33) Barsoum, M. W.; Radovic, M. *Annu. Rev. Mater. Sci.* **2011**, *41*, 195−227.
(34) Wang, X. H.; Zhou, Y. C. *J. Mater. Sci. Technol.* **2010**, *26*, 385−416.
(35) Eklund, P.; Beckers, M.; Jansson, U.; Högberg, H.; Hultman, L. *Thin Solid Films* **2010**, *518*, 1851−1878.
(36) Sun, Z. M. *Int. Mater. Rev.* **2011**, *56*, 143−166.
(37) Naguib, M.; Kurtoglu, M.; Presser, V.; Lu, J.; Niu, J.; Heon, M.; Hultman, L.; Gogotsi, Y.; Barsoum, M. W. *Adv. Mater.* **2011**, *23*, 4248−4253.
(38) Naguib, M.; Mashtalir, O.; Carle, J.; Presser, V.; Lu, J.; Hultman, L.; Gogotsi, Y.; Barsoum, M. W. *ACS Nano* **2012**, *6*, 1322−1331.
(39) Naguib, M.; Come, J.; Dyatkin, B.; Presser, V.; Taberna, P. -L.; Simon, P.; Barsoum, M. W.; Gogotsi, Y. *Electrochem. Commun.* **2012**, *16*, 61−64.
(40) Come, J.; Naguid, M.; Rozier, P.; Barsoum, M. W.; Gogotsi, Y.; Taberna, P. -L.; Morcrette, M.; Simon, P. *J. Electrochem. Soc.* **2012**, *159*, A1368−A1373.
(41) Kresse, G.; Furthmullerr, J. *Phys. Rev. B* **1996**, *54*, 11169−11186.
(42) Blöchl, P. E. *Phys. Rev. B* **1994**, *50*, 17953−17979.
(43) Perdew, J. P.; Burke, K.; Ernzerhof, M. *Phys. Rev. Lett.* **1996**, *77*, 3865−3868.
(44) Grimme, S. *J. Comput. Chem.* **2006**, *27*, 1787−1799.
(45) Henkelman, G.; Uberuaga, B. P.; Jónsson, H. *J. Chem. Phys.* **2000**, *113*, 9901−9904.
(46) Enyashin, A. N.; Ivanovskii, A. L. *Comput. Theor. Chem.* **2012**, *989*, 27−32.
(47) Aydinol, M. K.; Kohan, A. F.; Ceder, G.; Cho, K.; Joannopoulos, J. *Phys. Rev. B* **1997**, *56*, 1354−1365.
(48) Aydinol, M. K.; Ceder, G. *J. Electrochem. Soc.* **1997**, *144*, 3832−3835.
(49) Aydinol, M. K.; Kohan, A. F.; Ceder, G. *J. Power Sources* **1997**, *68*, 664−668.
(50) Meng, Y. S.; Arroyo-de Dompablo, M. E. *Energy Environ. Sci.* **2009**, *2*, 589−609.
(51) Yang, Z.; Choi, D.; Kerisit, S.; Rosso, K. M.; Wang, D.; Zhang, J.; Graff, G.; Liu, J. *J. Power Sources* **2009**, *192*, 588−598.
(52) Chen, Z.; Belharouak, I.; Sun, Y. -K.; Amine, K. *Adv. Funct. Mater.* **2012**, DOI: 10.1002/adfm.201200698.
(53) Koudriachova, M. V.; Harrison, N. M.; de Leeuw, S. W. *Solid State Ionics* **2002**, *152−153*, 189−194.
(54) Macklin, W. J.; Neat, R. J. *Solid State Ionics* **1992**, *53−56*, 694−700.
(55) Sun, C. H.; Yang, X. H.; Chen, J. S.; Li, Z.; Lou, X. W.; Li, C.; Smith, S. C.; Lu, G. Q.; Yang, H. G. *Chem. Commun.* **2010**, *46*, 6129−6131.
(56) Lunell, S.; Stashans, A.; Ojamäe, L.; Lindström, H.; Hagfeldt, A. *J. Am. Chem. Soc.* **1997**, *119*, 7374−7380.
(57) Olson, C. L.; Nelson, J; Islam, M. S. *J. Phys. Chem. B* **2006**, *110*, 9995−10001.
(58) Wagemaker, M.; van de Krol, R.; Kentgens, A. P. M.; van Well, A. A.; Mulder, F. M. *J. Am. Chem. Soc.* **2001**, *123*, 11454−11461.
(59) Lindström, H.; Södergren, S.; Solbrand, A.; Rensmo, H.; Hjelm, J.; Hagfeldt, A.; Lindquist, S.-E. *J. Phys. Chem. B* **1997**, *101*, 7710−7716.
(60) Koudriachova, M. V.; Harrison, N. M.; de Leeuw, S. W. *Phys. Rev. Lett.* **2001**, *86*, 1275−1278.
(61) van der Krol, R.; Goossens, A.; Meulenkamp, E. A. *J. Electrochem. Soc.* **1999**, *146*, 3150−3154.
(62) Toyoura, K.; Koyama, Y.; Kuwabara, A.; Tanaka, I. *J. Phys. Chem. C* **2010**, *114*, 2375−2379.
(63) Persson, K.; Sethuraman, V. A.; Hardwick, L. J.; Hinuma, Y.; Meng, Y. S.; van der Ven, A.; Srinivasan, V.; Kostecki, R.; Ceder, G. *J. Phys. Chem. Lett.* **2010**, *1*, 1176−1180.
(64) Persson, K.; Hinuma, Y.; Meng, Y. S.; Van der Ven, A.; Ceder, G. *Phys. Rev. B* **2010**, *82*, 125416.